Monthly Notices of the ROYAL ASTRONOMICAL SOCIETY

MNRAS **501,** 4064–4079 (2021)
Advance Access publication 2020 December 21

doi:10.1093/mnras/staa3907

Determining star formation rates in active galactic nuclei hosts via stellar population synthesis

Rogério Riffel,[1,2★] Nicolas D. Mallmann,[1,2] Gabriele S. Ilha,[2,3] Thaisa Storchi-Bergmann,[1,2] Rogemar A. Riffel,[2,3] Sandro B. Rembold,[2,3] Dmitry Bizyaev,[4,5] Janaina C. do Nascimento,[1,2] Jaderson S. Schimoia,[2,3] Luiz N. da Costa,[2,6] Nicholas Fraser Boardman,[7] Médéric Boquien[8] and Guilherme S. Couto[8]

[1]*Departamento de Astronomia, Instituto de Física, Universidade Federal do Rio Grande do Sul, CP 15051, 91501-970, Porto Alegre, RS, Brazil*
[2]*Laboratório Interinstitucional de e-Astronomia - LIneA, Rua Gal. José Cristino 77, Rio de Janeiro, RJ - 20921-400, Brazil*
[3]*Departamento de Física, Centro de Ciências Naturais e Exatas, Universidade Federal de Santa Maria, 97105-900, Santa Maria, RS, Brazil*
[4]*Apache Point Observatory and New Mexico State University, P.O. Box 59, Sunspot, NM 88349-0059, USA*
[5]*Sternberg Astronomical Institute, Moscow State University, 119992 Moscow, Russia*
[6]*Observatório Nacional - MCT, Rua General José Cristino 77, Rio de Janeiro, RJ - 20921-400, Brazil*
[7]*Department of Physics & Astronomy, University of Utah, Salt Lake City, UT 84112, USA*
[8]*Centro de Astronomía (CITEVA), Universidad de Antofagasta, Avenida Angamos 601, Antofagasta, Chile*

Accepted 2020 December 15. Received 2020 December 4; in original form 2020 October 12

ABSTRACT

The effect of active galactic nuclei (AGNs) feedback on the host galaxy, and its role in quenching or enhancing star formation, is still uncertain due to the fact that usual star formation rate (SFR) indicators – emission-line luminosities based on the assumption of photoionization by young stars – cannot be used for active galaxies as the ionizing source is the AGN. We thus investigate the use of SFR derived from the stellar population and its relation with that derived from the gas for a sample of 170 AGN hosts and a matched control sample of 291 galaxies. We compare the values of SFR densities obtained via the Hα emission line (ΣSFR$_{\rm Gas}$) for regions ionized by hot stars according to diagnostic diagrams with those obtained from stellar population synthesis (ΣSFR$_\star$) over the last 1 to 100 Myr. We find that the ΣSFR$_\star$ over the last 20 Myr closely reproduces the ΣSFR$_{\rm Gas}$, although a better match is obtained via the transformation: $\log(\Sigma{\rm SFR}_\star) = (0.872 \pm 0.004)\log(\Sigma{\rm SFR}_{\rm Gas}) - (0.075 \pm 0.006)$ (or $\log(\Sigma{\rm SFR}_{\rm Gas}) = (1.147 \pm 0.005)\log(\Sigma{\rm SFR}_\star) + (0.086 \pm 0.080)$), which is valid for both AGN hosts and non-active galaxies. We also compare the reddening obtained via the gas Hα/Hβ ratio with that derived via the full spectral fitting in the stellar population synthesis. We find that the ratio between the gas and stellar extinction is in the range $2.64 \leq A_{Vg}/A_{V\star} \leq 2.85$, in approximate agreement with previous results from the literature, obtained for smaller samples. We interpret the difference as being due to the fact that the reddening of the stars is dominated by that affecting the less obscured underlying older population, while the reddening of the gas is larger as it is associated with a younger stellar population buried deeper in the dust.

Key words: galaxies: active – galaxies: evolution – galaxies: ISM – galaxies: star formation – galaxies: stellar content.

1 INTRODUCTION

Present-day galaxies display a wide range of luminosities, sizes, stellar population properties, structure, kinematics, and gas content, being the endpoint of a ∼13.8 Gyr long process (Aghanim et al. 2020). These properties have been shaped by a series of processes, and, according to them, galaxies can roughly be divided in passive and star forming. The passive galaxies are not actively forming stars and host a red and old stellar population, while the star-forming galaxies are blue, hosting large fractions of young stellar populations. Such bi-modal behaviour is observed even at high redshifts ($z > 2.5$) where populations of passive galaxies are observed (e.g. Muzzin et al. 2013; Brammer et al. 2009).

The bi-modality of galaxies has been verified in a number of studies over the years (e.g. Baldry et al. 2004; Wetzel, Tinker & Conroy 2012; Kauffmann et al. 2003a; Noeske et al. 2007; van der Wel et al. 2014). However, it is not yet clear which mechanisms are driving the shutting down of star formation (SF) and transforming the blue star-forming spiral galaxies into *red-and-dead* galaxies. A major challenge in modern astrophysics is to determine the nature of the physical mechanism quenching SF in galaxies.

One mechanism that has been invoked by a number of studies is the feedback of active galactic nuclei (AGNs). AGN feedback can quench SF by heating and/or (re)moving the gas. AGN outflows are often considered as negative feedback processes that suppress SF (e.g. Granato et al. 2004; Fabian 2012; King & Pounds 2015; Zubovas & Bourne 2017; Trussler et al. 2020, and references therein). On the other hand, some models and simulations suggest that these outflows and jets can in some cases compress the galactic gas, and therefore

★ E-mail: riffel@ufrgs.br

© 2020 The Author(s)
Published by Oxford University Press on behalf of the Royal Astronomical Society

Downloaded from https://academic.oup.com/mnras/article/501/3/4064/6043241 by Universidade Federal do Rio Grande do Sul user on 07 April 2021

act as a catalyser and boosting the SF (e.g. Rees 1989; Hopkins 2012; Nayakshin & Zubovas 2012; Zubovas et al. 2013; Bieri et al. 2016; Zubovas & Bourne 2017) and even form stars inside the outflow (e.g. Ishibashi & Fabian 2012; Zubovas et al. 2013; El-Badry et al. 2016; Wang & Loeb 2018; for an observational example see Gallagher et al. 2019, and references therein).

Cosmological simulations (e.g. Springel et al. 2005; Vogelsberger et al. 2014; Crain et al. 2015) performed without the inclusion of feedback effects are not able to reproduce the galaxy luminosity function (at both the low and high-luminosity ends), and also underestimate the ages of the most massive galaxies (see figs 8 and 10 of Croton et al. 2006). It thus seems that effective feedback is required to reproduce the galaxy properties, but simulations can only provide limited insight into the nature and source of the feedback processes (e.g. AGN or SN dominated; Schaye et al. 2015). This is because there are still not enough observational constraints on these processes, and in particular, in the case of AGN, in order to verify how quenched is the SF it is necessary to robustly quantify the star formation rates (SFRs) of the hosts in the vicinity of the AGN. Both AGN activity and SF are regulated by the amount of available gas in the host galaxy. The relation between the gas and SF is relatively well characterized by previous studies (e.g. Kennicutt & Evans 2012; Lin et al. 2019; Barrera-Ballesteros et al. 2020; Zhuang & Ho 2020). Simulations should be able to correctly reproduce the observed SF; this, however, will depend on the efficiency of feedback processes in the interstellar medium (ISM). But resolving such processes is not yet possible in simulations of cosmological volumes (Schaye et al. 2015). In addition, in current models, the feedback processes are included in an ad hoc manner (Weinberger et al. 2017; Nelson et al. 2019), being activated by a threshold luminosity.

While there are many calibrators to determine the SFR for non-active galaxies (for a review, see Kennicutt 1998; Kennicutt & Evans 2012), in the case of AGN this is a very difficult task, since the emitting gas is ionized by the AGN radiation. Therefore, SFR indicators and equations calibrated with stellar photoionization prescriptions cannot be used in this context. Efforts have been made using far-infrared luminosities as SF indicators (e.g. Kennicutt et al. 2009; Rosario et al. 2013, 2016, 2018, and references therein) or mid-infrared neon ([Ne II] 12.81 μm and [Ne III] 15.56 μm) emission lines (Zhuang, Ho & Shangguan 2019). The infrared observations used in these works are obtained using large apertures, including the whole galaxy emission. As discussed in Rosario et al. (2016), despite finding a good correlation between far-infrared emission and SFR (which can be attributed to leaking of the SF regions to the whole galaxy or that the SF is constant over several hundreds of Myr) a substantial component of the cold dust luminosity that is associated with a diffuse interstellar radiation field can come from evolved stars. Even if the contribution from an old age stellar population is not dominant, the far-infrared may not be a good tracer of SF since dust can be heated by stars that are older than a few hundred Myr (Kennicutt et al. 2009; Hao et al. 2011; Rosario et al. 2016). Other recent effort on the bluer part of the spectrum has been made using a re-calibration [O II] λ3727 emission line (Zhuang et al. 2019; Zhuang, Ho & Shangguan 2020), which is metallicity and electron density dependent.

From the above, it is clear that it is thus necessary to find an independent way to obtain SFRs in AGN hosts. A powerful technique to disentangle the components summing up to a galaxy spectral energy distribution (SED) is stellar populations synthesis (e.g. Cid Fernandes et al. 2004, 2005; Riffel et al. 2009, 2008; Walcher et al. 2011; Baldwin et al. 2018; Cid Fernandes 2018; Salim, Boquien & Lee 2018; Peterken et al. 2020, and references therein). The synthesis is based on the simultaneous fit of different proportions of composite or simple stellar populations (SSPs) templates from a base of such spectra to the observed spectrum. In the case of the STARLIGHT fitting code (Cid Fernandes et al. 2004, 2005; Cid Fernandes 2018), it returns the values of the gas mass rate that has been converted into stars throughout the galaxy life as well as this rate for each single SSP included in the base. These values can therefore be used to compute the SFR via stellar population synthesis, $\mathrm{SFR}_\star$. In fact, this was already applied in Asari et al. (2007) using single fiber Sloan Digital Sky Survey (SDSS) data and older stellar population models generations (they used Bruzual & Charlot 2003 models).

From the discussion above, it is clear that it is of utmost importance to characterize the SFR of AGN hosts – in particular in the narrow-line region (NLR) and extended narrow-line region (ENLR), which are photoionized by the AGN. And in order to verify the actual role of the AGN on the SFR, it is necessary to compare the SFR values obtained for the NLR and ENLR with those obtained for a matched control sample of non-active galaxies at similar distances from the nucleus, as well as with predictions from simulations. In Rembold et al. (2017), we described the method we have used to select our sample of AGN and a matched control galaxy sample from the Mapping Nearby Galaxies at APO (MaNGA; Bundy et al. 2015) survey. Here, we have used an updated sample of 170 AGN and 291 controls (Deconto-Machado, in preparation), selected as in Rembold et al. (2017) to compute SFR indicators from the gas – using diagnostic diagrams to separate gas ionized by AGN and by hot stars – and from the stellar population synthesis and investigate the relation between them. We propose equations to relate the SFR densities obtained via emission lines, $\Sigma\mathrm{SFR}_{\mathrm{Gas}}$ with that obtained via stellar population synthesis, $\Sigma\mathrm{SFR}_\star$, allowing to obtain one from the other.

This paper is structured as follows: in Section 2, we present the updated samples. The methods used to determine the SFR are described in Section 3. The results are presented and discussed in Section 4 and conclusions are made in Section 5. We have used throughout the paper $H_0 = 67.7\,\mathrm{km\,s^{-1}\,Mpc^{-1}}$, $\Omega_m = 0.31$ (Aghanim et al. 2020).

2 DATA

The data used here were obtained from the MaNGA survey (Bundy et al. 2015). MaNGA is part of the fourth generation Sloan Digital Sky Survey (SDSS IV). The survey has provided optical spectroscopy (3600–10 400 Å) of ∼10 000 nearby galaxies (with $\langle z \rangle \approx 0.03$). The observations were carried out with fiber bundles of different sizes (19–127 fibers) covering a field of 12 arcsec to 32 arcsec in diameter. MaNGA observations are divided into 'primary' and 'secondary' targets, the former are observed up to 1.5 effective radius (R_e) while the latter is observed up to 2.5 R_e. For more details, see Drory et al. (2015), Law et al. (2015), and Yan et al. (2016a, b).

The sample used in this work is an update of our previous MaNGA AGN hosts and matched non-active control galaxies (Rembold et al. 2017). The control sample was selected in order to match the AGN hosts in terms of stellar mass, redshift, visual morphology, and inclination (for details, see Rembold et al. 2017). After the release of the MaNGA Product Launch 8 (MPL-8; Gunn et al. 2006; Smee et al. 2013; Bundy et al. 2015; Drory et al. 2015; Law et al. 2015, 2016; Yan et al. 2016a, b; Blanton et al. 2017; Wake et al. 2017; Aguado et al. 2019; Belfiore et al. 2019; Cherinka et al. 2019; Westfall et al. 2019), the number of observed AGN with MaNGA has grown to 170 AGNs using the same criteria as in Rembold et al. (2017). For each AGN, we have also selected two control galaxies. Since more than one AGN host can share the same control galaxy, this inactive

Downloaded from https://academic.oup.com/mnras/article/501/3/4064/6043241 by Universidade Federal do Rio Grande do Sul user on 07 April 2021

sample is composed by 291 sources. Both AGN and control samples are located in the redshift range $0.02 \lesssim z \lesssim 0.15$, and their typical stellar masses are of the order of $10^{10.5}$–10^{11} $M_\odot$. Most AGN in our sample (64 per cent) are low-luminosity, presenting [O III] λ5007 Å luminosities below 3.8×10^{40} erg s^{-1}.

Analysis of the morphological classification of galaxies in our sample with the Galaxy Zoo data base (Lintott et al. 2008, 2011) reveals that our updated AGN sample contains 57 early-type (33.5 percent), 87 late-type (51.2 percent), three merger galaxies (1.8 percent), and 23 objects (13.5 percent) without classification. The control sample is composed of 125 early-type (36.8 percent), 182 late-type (53.5 percent), four merger galaxies (1.2 percent), and 29 objects (8.5 percent) whose classifications are uncertain. Regarding nuclear activity, 63.6 percent of the AGN host sample presents Seyfert nuclei, while the other 36.4 percent are low-ionization nuclear emission-line region (LINER) sources. For more details on the updated sample properties, see Deconto-Machado (in preparation).

For all galaxies in our sample, gas and stellar population parameters have been derived from the MaNGA IFU optical spectra datacubes. We refer to Bundy et al. (2015) for details on the MaNGA spectroscopic data, like spectral resolution, spatial coverage, and pixel scale.

3 STAR FORMATION RATES

We have obtained the SFR surface densities for the gas $\Sigma\mathrm{SFR}_{\mathrm{Gas}}$ and for the stars $\Sigma\mathrm{SFR}_\star$ for each spaxel of the datacubes dividing the corresponding SFR values in units of solar masses per year ($M_\odot$ yr^{-1}) by the area of each spaxel in kpc^2.

Our goal is to compare SFR values obtained from the gas emission lines to those obtained from stellar population synthesis. As the prescriptions for the gas are based on the assumption that it is photoionized by young, hot stars, this comparison needs to be done only for spaxels in which the gas is indeed ionized by stars. We have thus used optical diagnostic diagrams (see Section 3.1) to isolate the spaxels whose emission is produced by photoionization by the radiation of young stars.

We also need to be sure that the signal-to-noise ratio (SNR) of the data from each spaxel is high enough to allow reliable measurements. In summary, in order to ensure that the measurements are accurate, we have subjected the results obtained for each spaxel to the validation criteria listed below.

3.1 Spaxels validation

We considered results from a spaxel to be valid only if they match the following criteria:

(i) The mean value of the SNR in the continuum window between 5650 and 5750 Å is ≥10. This was applied in order to ensure that the stellar population fits are reliable (Cid Fernandes et al. 2004, 2005; Riffel et al. 2009);

(ii) The Hα equivalent width (EW) is larger than 10 Å and the Hβ EW is larger than 3 Å. This is necessary in order to avoid spaxels that could have large contribution from other ionizing sources such as post-AGB stars;

(iii) The following relation between line ratios is obeyed: $\log([O\,\mathrm{III}]\lambda5007/\mathrm{H}\beta) < 0.61/(\log([N\,\mathrm{II}]\lambda6583/\mathrm{H}\alpha) - 0.05) + 1.3$ (Kauffmann et al. 2003b). This is based on diagnostic diagrams to ensure that only star-forming emission spaxels are being used in the calculation of the SFR.

By using these selection criteria, we make sure that we are only using results obtained for spaxels that have a good stellar population fit and the gas is photoionized by hot young stars.

3.2 SFR from stellar population synthesis

Our first step was to perform a full spectral fitting stellar population synthesis on our datacubes. We used the STARLIGHT fitting code (Cid Fernandes et al. 2005; Cid Fernandes 2018) that combines the spectra of a base of $N_\star$ SSP template spectra $b_{j,\lambda}$, in different proportions, in order to reproduce the observed spectrum O_λ. For this comparison, the modelled spectra M_λ are normalized at a user-defined wavelength (λ_0). The reddening is given by the term $r_\lambda = 10^{-0.4(A_\lambda - A_{\lambda_0})}$, weighted by the population vector x_j (which represents the fractional contribution of the jth SSP to the light at the normalization wavelength λ_0), and convolved with a Gaussian distribution $G(v_\star, \sigma_\star)$ to account for velocity shifts $v_\star$, and velocity dispersion $\sigma_\star$.

Each model spectrum can be expressed as

$$M_\lambda = M_{\lambda_0}\left[\sum_{n=1}^{N_\star} x_j\, b_{j,\lambda}\, r_\lambda\right] \otimes G(v_\star, \sigma_\star), \quad (1)$$

where M_{λ_0} is the flux of the synthetic spectrum at the wavelength λ_0. To find the best parameters for the fit, the code searches for the minimum of $\chi^2 = \sum_{\lambda_i}^{\lambda_f}[(O_\lambda - M_\lambda)\omega_\lambda]^2$, where ω_λ is the inverse of the error, using a simulated annealing plus Metropolis scheme. We normalized our data at λ_0, adopted to be the mean value between 5650 and 5750 Å. The reddening law we have used was that of Cardelli, Clayton & Mathis (1989) and the synthesis was performed for the spectral range from 3700 to 6900 Å.

The SSPs base set we use is the *GM* described in Cid Fernandes et al. (2013, 2014) that is constructed using the MILES (Vazdekis et al. 2010) and González Delgado et al. (2005) models. We have updated it with the MILES V11 models (Vazdekis et al. 2016). We used 21 ages (t = 0.001, 0.006, 0.010, 0.014, 0.020, 0.032, 0.056, 0.1, 0.2, 0.316, 0.398, 0.501 0.631, 0.708, 0.794, 0.891, 1.0, 2.0, 5.01, 8.91, and 12.6 Gyr) and four metallicities (Z = 0.19, 0.40, 1.00, and 1.66 $Z_\odot$). We have also added to the spectral base a power law of the form $F_\nu \propto \nu^{-1.5}$ to account for the contribution of a possible AGN continuum (observed directly or as scattered light).

Since STARLIGHT is not prepared to handle with datacubes, we have used our in house software MEGACUBE (Mallmann et al. 2018). This code wraps STARLIGHT to deal with its numerous input and output files involved with IFU data. Each spaxel requires an ASCII file and generates another one. For each galaxy, thousands of files are organized and extracted to a coherent datacube to be subsequently analysed. The code can also be used for a multitude of functions since it was developed with modular capabilities, i.e. parts of the software can be changed, swapped, or removed depending on the scientific goals. Besides allowing us to easily prepare and fit the stellar populations in datacubes, its modular approach allows to use MEGACUBE to generate maps for the direct and indirect STARLIGHT fitting products. See Mallmann et al. (2018) for further details.

One of the data products computed by MEGACUBE is the SFR obtained from the stellar fit ($SFR_\star$) over a user-defined age interval ($\Delta t = t_{j_f} - t_{j_i}$). This can be computed since the SSPs model spectra are in units of $L_\odot$ Å^{-1} $M_\odot^{-1}$, and the observed spectra (O_λ) are in units of erg/s/cm^2/Å (for details, see the STARLIGHT manual[1]). The $\mathrm{SFR}_\star$

[1] http://www.starlight.ufsc.br/

Downloaded from https://academic.oup.com/mnras/article/501/3/4064/6043241 by Universidade Federal do Rio Grande do Sul user on 07 April 2021

over the chosen Δt can be computed assuming that the mass of each base component (j) that has been processed into stars can be obtained as

$$M_{\star,j}^{\rm ini} = \mu_j^{\rm ini} \times \frac{4\pi d^2}{3.826 \times 10^{33}}, \quad (2)$$

where $M_{\star,j}^{\rm ini}$ is given in $M_\odot$, $\mu_j^{\rm ini}$ represents the mass that has been converted into stars for the jth element and its flux. This parameter is given in $M_\odot$ erg s^{-1} cm^{-2}; d is the distance to the galaxy in cm and 3.826×10^{33} is the Sun's luminosity in erg s^{-1}. Thus, the SFR over the Δt as defined above can be obtained from the equation:

$$\mathrm{SFR}_\star = \frac{\sum_{ji}^{jf} M_{\star,j}^{\rm ini}}{\Delta t}. \quad (3)$$

For more details, see the STARLIGHT manual[1], and for an application example, see Asari et al. (2007) and Riffel, Zakamska & Riffel (2020).

3.3 SFR from Hα emission-line fluxes

A very common approach to determine SFR from the gas emission ($\mathrm{SFR_{Gas}}$) is using hydrogen recombination emission-line fluxes (see Kennicutt 1998; Kennicutt & Evans 2012, for a review). Therefore, we have used the MEGACUBE absorption free emission-line datacubes to fit the emission lines. This procedure was done using the IFSCUBE[2] tool: a python package designed to perform analysis tasks in datacubes. This code allows to fit emission lines with Gaussian functions (among other options), allowing to constraint kinematics and line fluxes ratios in a very robust and easy way (Ruschel-Dutra 2020).

We use the IFSCUBE Python package to fit the emission-line profiles of Hβ, [O III] $\lambda\lambda$4959, 5007, He I λ5876, [O I] λ6300, Hα [N II] $\lambda\lambda$6548, 6583, and [S II] $\lambda\lambda$6716, 6731. We fit the spectra after the subtraction of the underlying stellar population contribution derived in the previous section. The line profiles are fitted with Gaussian curves by adopting the following constraints: (i) the width and centroid velocities of emission lines from the same parent ion are tied; (ii) the [O III] λ5007/λ4959 and [N II] λ6583/λ6548 flux ratios are fixed to their theoretical values of 2.98 and 3.06, respectively; (iii) the centroid velocity is allowed to vary from –300 to 300 km s^{-1} for [S II] lines and –350 to 350 km s^{-1} for the other lines relative to the velocity obtained from the redshift of each galaxy (listed in the MaNGA Data Analysis Pipeline – DAP); and (iv) the observed velocity dispersion of all lines is limited to the range of 40–300 km s^{-1}. In addition, we include a first-order polynomial to reproduce the local continuum.

Since emission lines effectively re-emit the photons absorbed from the integrated stellar Lyman continuum, they provide a direct probe of the population of young, massive stars. Maps for the $\mathrm{SFR_{Gas}}$ were obtained with the following equation from Kennicutt (1998):

$$\mathrm{SFR_{Gas}}(M_\odot/\mathrm{yr}) = 7.9 \times 10^{-42} L(\mathrm{H}\alpha)(\mathrm{erg\,s^{-1}}), \quad (4)$$

were $L(\mathrm{H}\alpha)$ is the reddening corrected Hα luminosity.

3.4 Stellar population and nebular reddening

STARLIGHT models the reddening of the integrated stellar continuum as a foreground dust screen and it is parametrized by the extinction in the V-band, A_V using the reddening law of Cardelli et al. (1989).

[2]https://ifscube.readthedocs.io/en/latest/

The gas reddening was obtained considering Case B recombination at $T_e = 10\,000$ K (Kennicutt 1998), and the corresponding colour excess $E(B-V)$ can be obtained as follows (see Calzetti et al. 2000; Domínguez et al. 2013):

$$E(B-V) = \frac{E(\mathrm{H}\beta - \mathrm{H}\alpha)}{f_\lambda(\mathrm{H}\beta) - f_\lambda(\mathrm{H}\alpha)} \quad (5)$$

$$= \frac{2.5}{R_\lambda\,(f_\lambda(\mathrm{H}\beta) - f_\lambda(\mathrm{H}\alpha))} \left[\frac{(F_{\mathrm{H}\alpha}/F_{\mathrm{H}\beta})^{\rm obs}}{(F_{\mathrm{H}\alpha}/F_{\mathrm{H}\beta})^{\rm int}}\right], \quad (6)$$

where $f_\lambda(\mathrm{H}\alpha)$ and $f_\lambda(\mathrm{H}\beta)$ are the reddening curve values at the Hα and Hβ wavelengths, which for the CCM's reddening law are $f_\lambda(\mathrm{H}\alpha) = 0.818$ and $f_\lambda(\mathrm{H}_\beta) = 1.164$.

Adopting $R_\lambda = R_V = 3.1$ and the theoretical line ratio of $F_{\mathrm{H}\alpha}/F_{\mathrm{H}\beta} = 2.86$ for case B H I recombination for an electron temperature of $T_e = 10\,000$ K and electron density of $N_e = 100$ cm^{-3} (Osterbrock & Ferland 2006), we obtain

$$A_V = 7.22\ \log\left(\frac{(F_{\mathrm{H}\alpha}/F_{\mathrm{H}\beta})^{\rm obs}}{2.86}\right). \quad (7)$$

The intrinsic flux ($F_{\rm int}^\lambda$) of an emission line is then related to the observed one ($F_{\rm obs}^\lambda$) by the following equation

$$F_{\rm int}^\lambda = F_{\rm obs}^\lambda 10^{0.4A_\lambda} \quad (8)$$

$$= F_{\rm obs}^\lambda 10^{0.4R_\lambda E(B-V)}, \quad (9)$$

where A_λ is the extinction at wavelength λ and R_λ is the extinction curve index from Cardelli et al. (1989). The equation above was used to correct the Hα emission-line flux used in the calculation of the Hα luminosity and $\mathrm{SFR_{Gas}}$.

4 RESULTS AND DISCUSSION

4.1 Comparison between $SFR_{\rm Gas}$ and SFR_*

In order to compare the SFR values obtained for all galaxies that are at different distances, we have calculated the SFR surface densities $\Sigma\mathrm{SFR}_\star$ and $\Sigma\mathrm{SFR_{Gas}}$ by dividing the obtained SFRs values for each spaxel by its area in kpc^2. The resulting values are in units of $M_\odot$ yr^{-1} kpc^{-2}.

The $\Sigma\mathrm{SFR}_\star$ values were calculated over different age bins, comprising values over the last 1, 5, 10, 14, 20, 30, 56, and 100 Myr, each age bin corresponding to the added contribution of all younger age bins. These $\Sigma\mathrm{SFR}_\star$ values are compared to the $\Sigma\mathrm{SFR_{Gas}}$ ones in Fig. 1 for the total sample (sum of AGN and control samples) and in Fig. 2 for the SF spaxels only in the AGN hosts. We also present the identity line (e.g. x=y; dotted blue) together with a linear fit to the data points (solid red line) obtained using bootstrap realizations (Davison & Hinkley 1997) with Huber Regressor model that is robust to outliers (Owen 2007). The Spearman's correlation coefficient (r) and the number of spaxels are also included in the panels showing the plots.

What emerges from this exercise is that the best correlation ($r = 0.62$ for SF of the control + AGN samples and $r = 0.80$ if only SF spaxels in the AGN sample are considered) is obtained when comparing the $\Sigma\mathrm{SFR}_\star$ over the last 20 Myr with that obtained with $\Sigma\mathrm{SFR_{Gas}}$ (from the Hα emission line). Also, their values are close to a one to one relation, with $\log(\Sigma\mathrm{SFR}_\star) = (0.79 \pm 0.006)\log(\Sigma\mathrm{SFR_{Gas}}) - (0.22 \pm 0.009)$. This is also the stellar population age range that shows the smallest scatter of the points compared with the $\Sigma\mathrm{SFR}_\star$ derived over the other Δt's. This result is not surprising since the good agreement between the $\Sigma\mathrm{SFR_{Gas}}$ and $\Sigma\mathrm{SFR}_\star$ over the last

Downloaded from https://academic.oup.com/mnras/article/501/3/4064/6043241 by Universidade Federal do Rio Grande do Sul user on 07 April 2021

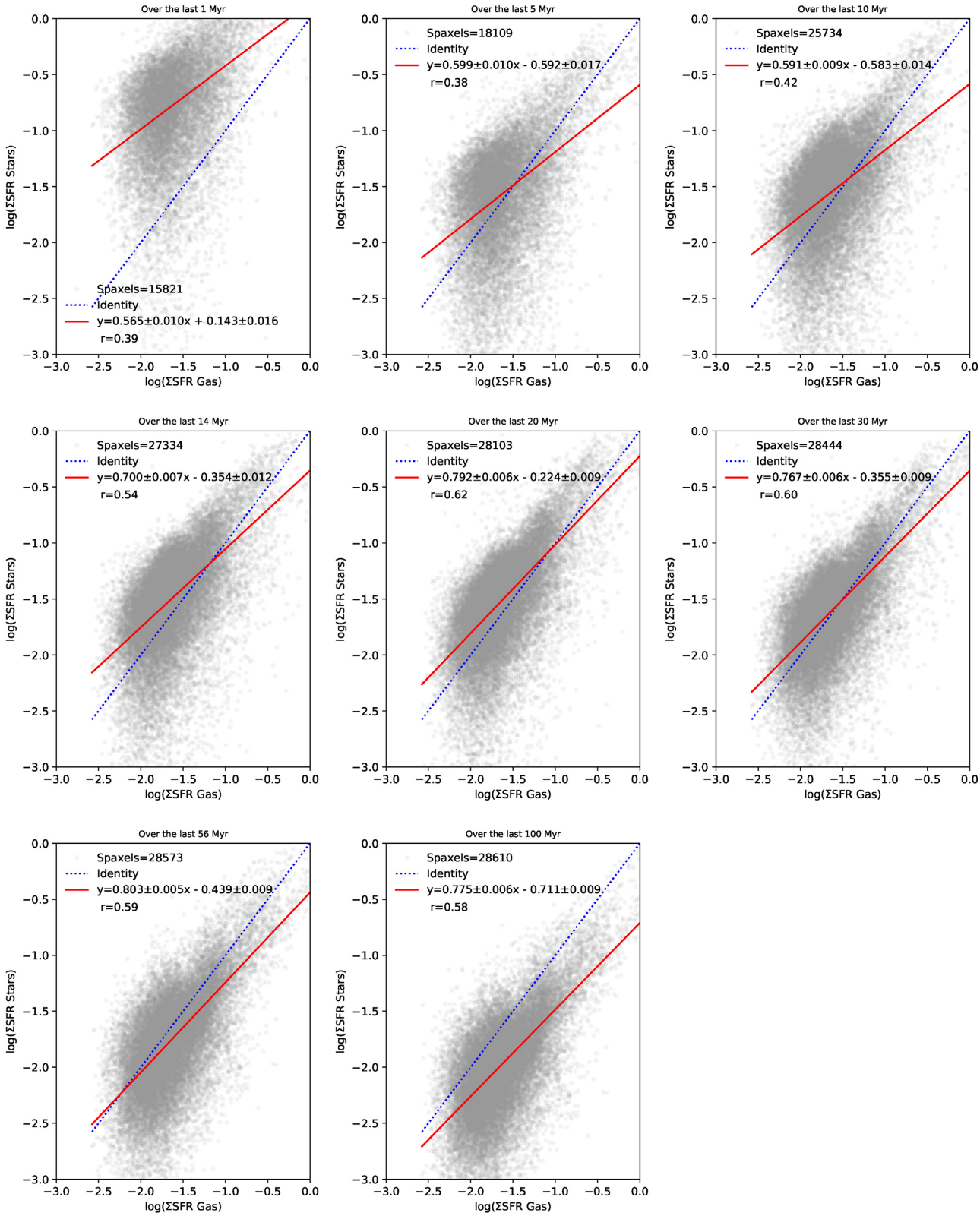

Figure 1. Comparison of ΣSFR_{Gas} with $\Sigma SFR_{\star}$ in logarithm units of $M_{\odot}\ yr^{-1}\ kpc^{-2}$ over the last 1, 5, 10, 14, 20, 30, 56, and 100 Myr, for all spaxels of the AGN and control samples obeying the criteria of Section 3.1. The red line is the linear relation of a robust fit between $\log(\Sigma SFR_{Gas})$ and $\log(\Sigma SFR_{\star})$ given inside the panels. We also list the number of spaxels and the Spearman's correlation coefficient (r) of the relation. For more details see text.

Downloaded from https://academic.oup.com/mnras/article/501/3/4064/6043241 by Universidade Federal do Rio Grande do Sul user on 07 April 2021

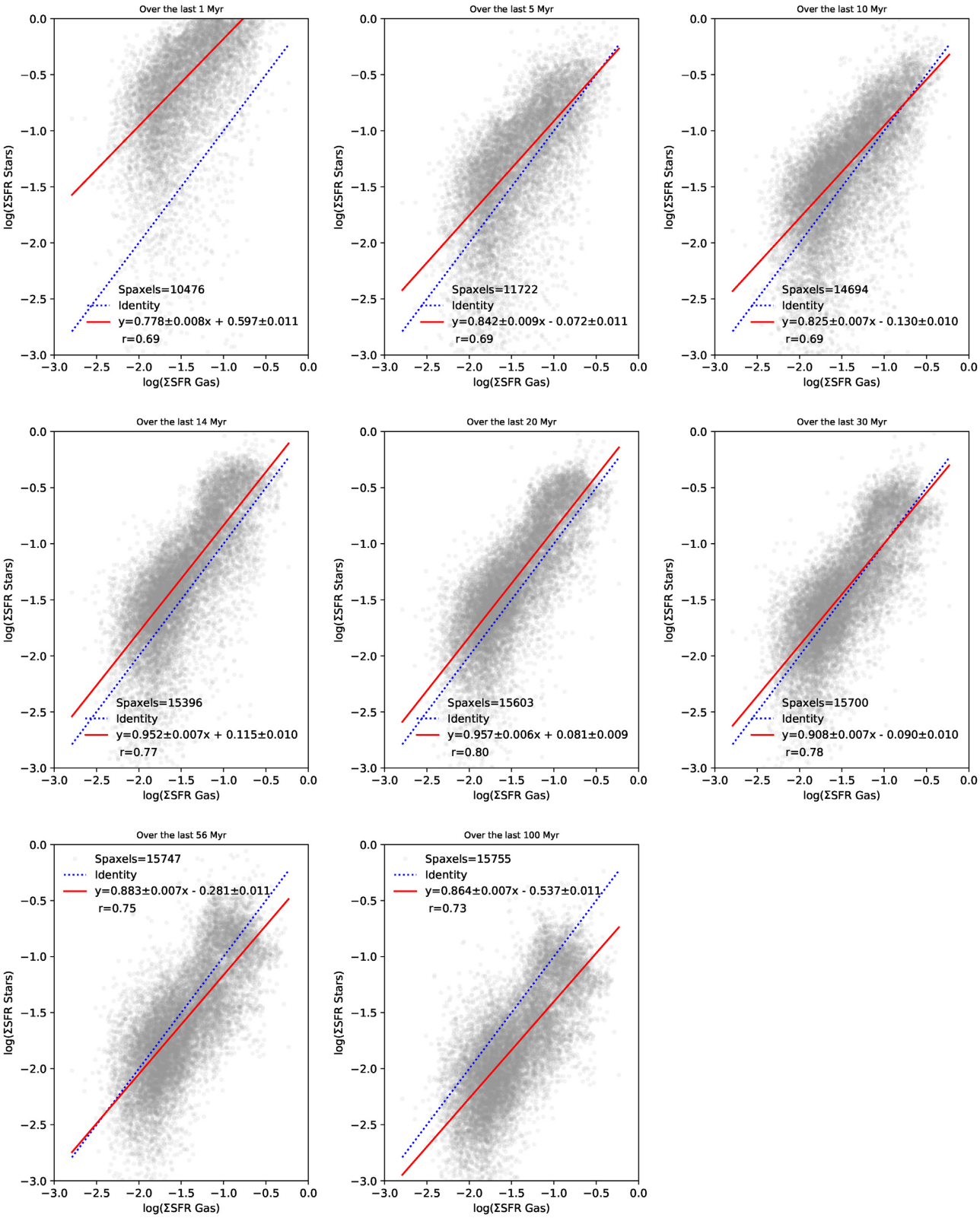

Figure 2. Same as Fig. 1 but only for the star-forming spaxels in the AGN sample.

Downloaded from https://academic.oup.com/mnras/article/501/3/4064/6043241 by Universidade Federal do Rio Grande do Sul user on 07 April 2021

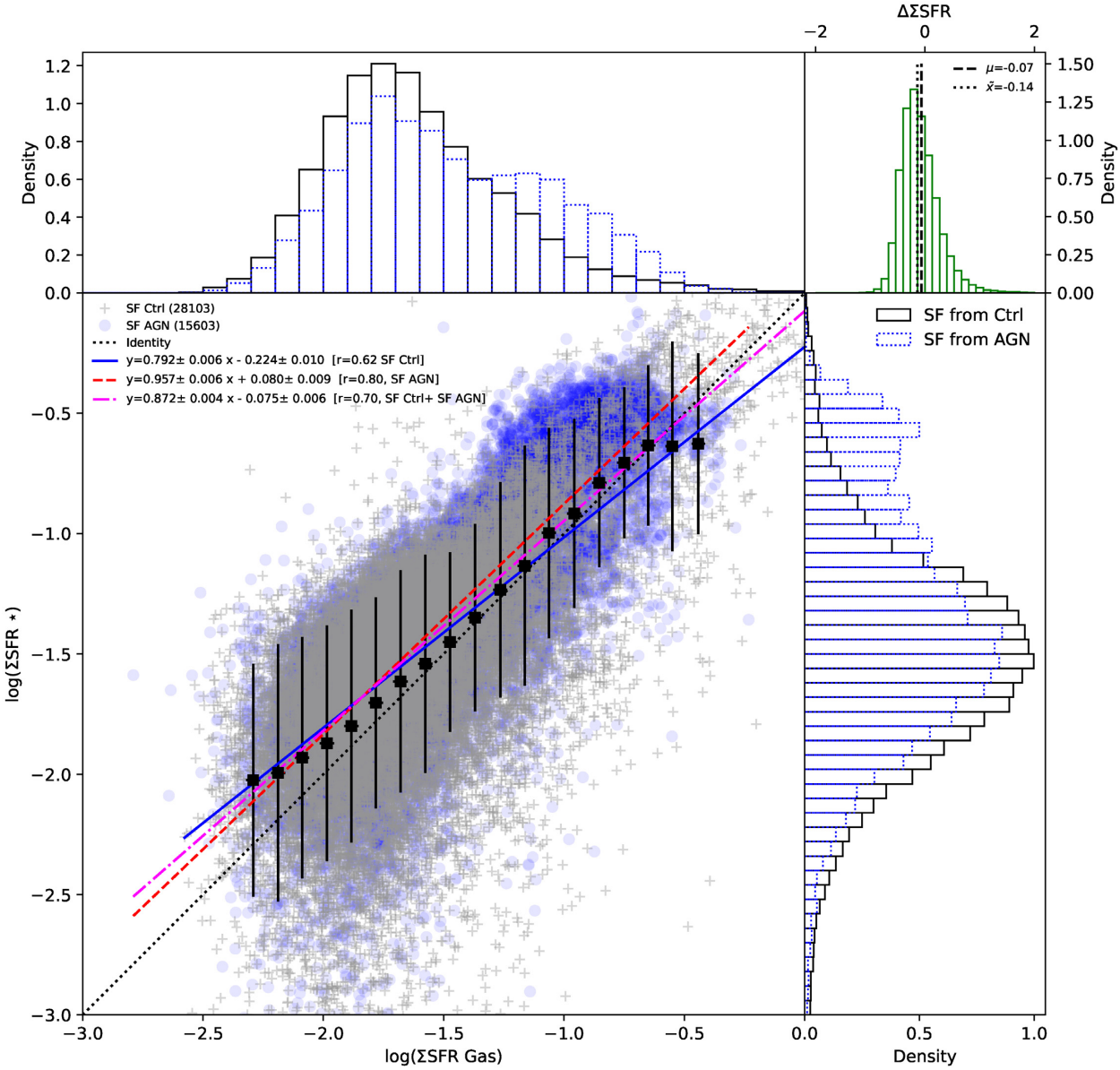

Figure 3. $\Sigma SFR_\star$ *versus* ΣSFR_{Gas} over the last 20 Myr in log scale. Spaxels with SF line ratios taken from the control sample ('Ctrl') are represented as grey plus symbols, SF spaxels taken from AGN hosts as light blue circles. Regressions for each data set are labelled. Squares represent the mean value with standard deviations of 20 linearly spaced bins over $\log(\Sigma SFR_{Gas})$ (values below 0.5 and 99.5 of the q-th percentile were removed) considering all spaxels (SF Ctrl and SF AGN). Density histograms for ΣSFR_{Gas} and $\Sigma SFR_\star$ of both samples are also shown. The top right histogram shows the $\Delta\Sigma = \log(\Sigma SFR_{Gas}) - \log(\Sigma SFR_\star)$ as well as the mean (μ) and median ($\tilde{x}$) values of this difference.

20 Myr is related to the fact that the stars that dominate the total ionizing photons budget are the hot, massive ($M > 10\ M_\odot$) and short-lived ($t < 20$ Myr) stars. Thus, as the emission-line fluxes provide an 'instantaneous' measure of the SFR (Kennicutt 1998), the corresponding SFR values should be more similar to those obtained from recent $SFR_\star$. In fact, our results are in agreement with the previous findings of Asari et al. (2007, see also Stasińska et al. 2015 and González Delgado et al. 2016) who found that the $SFR_\star$ of the last 25 Myr correlates well with that derived via nebular emission when using SDSS single fibber observations.

The above finding shows that one can use the $\Sigma SFR_\star$ over the last 20 Myr as a probe of the recent, instantaneous SFR that a galaxy is experiencing.

In order to investigate any possible difference in behaviour between the spaxels from the AGN host galaxies and those from the control galaxies, we have plotted in Fig. 3 the ΣSFR_{Gas} *versus* $\Sigma SFR_\star$ over the last 20 Myr (for spaxels with SF line ratios) as grey plus symbols for the control sample and as light blue circles for the AGN hosts. We also plot the mean values, with standard deviations, considering all the spaxels (both from control and AGN galaxies) divided in 20 linearly spaced bins over ΣSFR_{Gas}. Values below the 0.5th percentile and above the 99.5th percentile were removed to better display the results. The identity line (dotted black) is shown, as well as separate regressions for the two samples (AGN and control) and for their combined sample. We also show histograms

Downloaded from https://academic.oup.com/mnras/article/501/3/4064/6043241 by Universidade Federal do Rio Grande do Sul user on 07 April 2021

for the density distribution[3] of $\Sigma\mathrm{SFR}_{\mathrm{Gas}}$ and $\Sigma\mathrm{SFR}_{\star}$ for both samples, as well as a histogram showing the $\Delta\Sigma = \log(\Sigma\mathrm{SFR}_{\mathrm{Gas}}) - \log(\Sigma\mathrm{SFR}_{\star})$ together with the mean (μ) and median ($\tilde{x}$) values of this difference.

Besides obtaining the linear regressions to the data, as described above, we derived the Spearman's correlation coefficients, which are also listed within the Figs 1 and 3 panels. These figures show that: (i) when considering only SF spaxels from the control sample we found $\log(\Sigma\mathrm{SFR}_{\star}) = (0.792 \pm 0.006)\log(\Sigma\mathrm{SFR}_{\mathrm{Gas}}) - (0.224 \pm 0.010)$ with $r = 0.62$; (ii) when using the SF spaxels from the AGN hosts we found $\log(\Sigma\mathrm{SFR}_{\star}) = (0.957 \pm 0.006)\log(\Sigma\mathrm{SFR}_{\mathrm{Gas}}) + (0.080 \pm 0.009)$ with $r = 0.80$; and (iii) finally when combining both samples we find $\log(\Sigma\mathrm{SFR}_{\star}) = (0.872 \pm 0.004)\log(\Sigma\mathrm{SFR}_{\mathrm{Gas}}) - (0.075 \pm 0.006)$ with $r = 0.70$. The three best-fitting lines in Fig. 3 show a very similar slope, and a nearly one to one correlation is found. The difference histogram ($\Delta\Sigma\mathrm{SFR}$) confirms that both ΣSFRs are very similar, with the bulk of the differences being concentrated around $\sim$0. This result suggests that the $\Sigma\mathrm{SFR}_{\star}$ over the last 20 Myr can be directly used as a measure of the $\Sigma\mathrm{SFR}_{\mathrm{Gas}}$, for both star forming and AGN hosts (when the spaxel line ratios indicate SF excitation).

At the highest $\Sigma\mathrm{SFR}_{\mathrm{Gas}}$ and $\Sigma\mathrm{SFR}_{\star}$ values, there is a clear excess of AGN SF spaxels relative to those from the control ones (histograms in Fig. 3). In order to understand the origin of this excess, our first step was to remove the strong AGNs, defined as the sources with $L([\mathrm{O\,III}]\lambda5007\text{Å}) \geq 3.8 \times 10^{40}\,\mathrm{erg\,s^{-1}}$ (Rembold et al. 2017; Mallmann et al. 2018,) from our sample, since, if both the AGN activity and the SF would be driven by the same mechanism (e.g. larger gas reservoirs both forming stars and feeding the AGN) this could explain this excess. However, after the removal of these objects, the same trend remains and the excess is still observed. In order to identify the galaxies responsible for the excess, we applied a cut for high ΣSFRs. Selecting only spaxels with $\log(\Sigma\mathrm{SFR}_{\mathrm{Gas}}) > -1.0$ and $\log(\Sigma\mathrm{SFR}_{\star}) > -0.75$, we found that all the spaxels presenting these high values come from only four AGN hosts identified by the following MaNGA-IDs: 1-189584, 1-604022, 1-258373, 1-229731 (Figs A1–A4). Of these, only objects 1-258373 and 1-229731 are strong AGNs. This result shows that not only strong AGNs are producing the high ΣSFRs in Fig. 3.

Since a tight correlation between the SFR and the stellar mass of galaxies is expected, and indeed observed in the form of the so-called *SF main sequence* (MS) of galaxies (Brinchmann et al. 2004; Noeske et al. 2007; Daddi et al. 2007; Speagle et al. 2014; it is also observed when considering individual spaxels, e.g. Lin et al. 2019), we decided to normalize the ΣSFRs to the stellar mass, $M_{\star}$, of each spaxel. The result of this normalization is shown in Fig. 4, where one clearly sees that the spaxels contributing to the tail observed in the distributions of the AGN spaxels in the previous histograms are those with the highest $\Sigma\mathrm{SFR}/\mathrm{M}_{\star}$, and they clearly populate a separate region in this figure.

In order to investigate the origin of these high $\Sigma\mathrm{SFR}/M_{\star}$'s, we have tracked them back to the sources originating such spaxels. Therefore, using Fig. 4 we defined the limits of the high-$\Sigma\mathrm{SFR}/M_{\star}$ 'cloud' as $\log(\Sigma\mathrm{SFR}_{\mathrm{Gas}}/M_{\star}) > -8.2$ and $\log(\Sigma\mathrm{SFR}_{\star}/M_{\star}) > -7.8$ (cyan rectangle). The spaxels located in this region are from four AGNs, identified by the MANGAIDs: 1-189584, 1-604022 (these two being also identified as producing the high values in Figs 1 and 3, plus 1-603941, 1-420924, none of which is classified as strong AGNs.

This result suggests that these sources are somewhat particular in the sense of having a significantly larger star-forming gas reservoir leading to a higher SFR than the other sources in our sample. Interestingly, all these sources present companions or satellite galaxies at projected distances smaller than 70 kpc. In addition, objects 1-189584, 1-604022, and 1-603941 are members of galaxy groups (Fouque et al. 1992; White et al. 1999; Von Der Linden et al. 2007). This suggests that the higher SF efficiencies shown by these objects relative to other galaxies of similar masses are due to interactions with nearby galaxies. A definitive answer to this question requires a complete statistics of the environment of all galaxies in the sample, which is beyond the scope of this work but will be addressed in a forthcoming publication.

The results presented here clearly show that we can use the transformation equation:

$$\log(\Sigma\mathrm{SFR}_{\star}) = (0.872 \pm 0.004)\log(\Sigma\mathrm{SFR}_{\mathrm{Gas}}) - (0.075 \pm 0.006) \tag{10}$$

or

$$\log(\Sigma\mathrm{SFR}_{\mathrm{Gas}}) = (1.147 \pm 0.005)\log(\Sigma\mathrm{SFR}_{\star}) + (0.086 \pm 0.080)$$

to obtain the gas ΣSFR from the stellar one.

The above result is particularly useful for obtaining SFR values in the NLR or extended NLR (ENLR) of AGN hosts. Since the synthesis technique allows to fit the stellar populations disentangling it from the AGN featureless continuum, it is possible to use it to obtain the SFRs that one would derive from the gas emission, even in regions dominated by the AGN excitation, such as the NLR and ENLR, for which H I emission cannot be used as an SF indicator.

These results can thus be used to investigate if there is, for example, SF quenching (or SF enhancement) in the vicinity of AGN, comparing the results with the predictions of AGN feedback effects in cosmological simulations (e.g. Nelson et al. 2015; McAlpine et al. 2016). In a forthcoming publication, we intend to apply the relation of equation (10) in order to compare the ΣSFR we obtain in regions dominated by AGNs excitation to those obtained at similar distances from the nucleus for control galaxies in order to investigate any difference related to the AGN. The results will then be compared to those of cosmological simulation predictions (Schimoia et al., in preparation). In addition, we will extend the investigation previously done for a smaller sample (Mallmann et al. 2018) on the systematic stellar population differences between AGN hosts and controls for the updated sample used here (Mallmann et al., in preparation).

4.2 Comparing the nebular and stellar population reddening

A comparison between the A_V values obtained via H α/H β line ratios and that from the full spectral fitting of the stellar population is shown in Fig. 5. We fitted linear regressions to the data and derived the Spearman's correlation coefficients. We found that (i) when considering only SF spaxels from the control sample $A_{V,\star} = (0.379 \pm 0.003)A_{V,g} - (0.050 \pm 0.004)$, with $r = 0.60$; (ii) when using the SF spaxels from the AGN hosts, $A_{V,\star} = (0.352 \pm 0.005)A_{V,g} - (0.015 \pm 0.006)$, with $r = 0.55$; and (iii) when considering the combined samples of AGN and controls we find $A_{V,\star} = (0.370 \pm 0.003)A_{V,g} - (0.039 \pm 0.003)$, with $r = 0.58$.

This result suggests that the reddening derived via stellar population full spectral fitting is consistent for both samples and that the

[3]The counts are normalized to form a probability density, i.e. the integral under the histogram is 1. This is achieved by dividing the count by the number of observations times the bin width and not dividing by the total number of observations. The density histograms were obtained setting `density=True` in Python's MATPLOTLIB.PYPLOT.HIST routine.

Downloaded from https://academic.oup.com/mnras/article/501/3/4064/6043241 by Universidade Federal do Rio Grande do Sul user on 07 April 2021

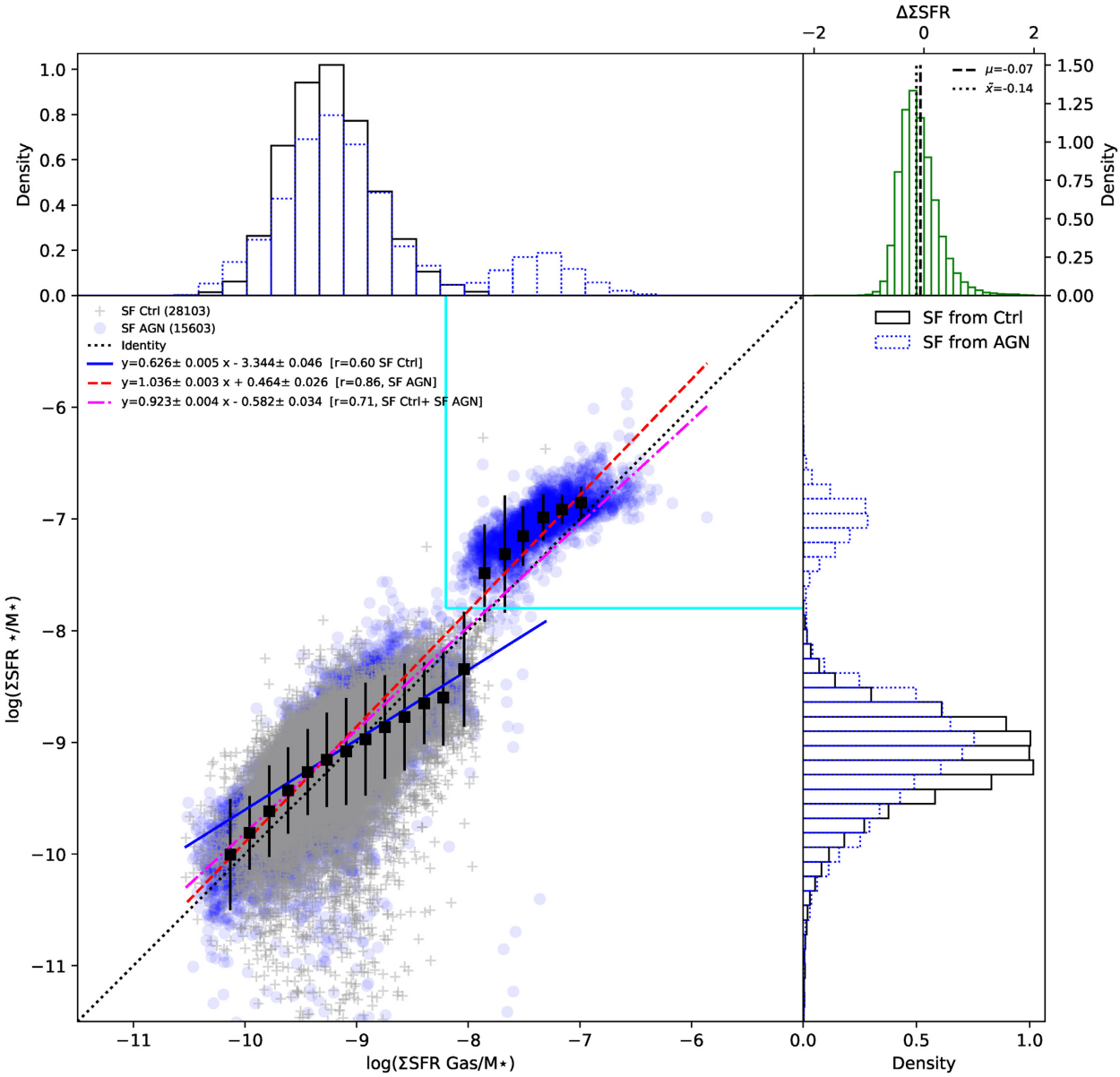

Figure 4. $\Sigma\mathrm{SFR}_{\mathrm{Gas}}$ *versus* $\Sigma\mathrm{SFR}_{\star}$ over the last 20 Myr normalized by stellar mass. Spaxels with SF line ratios taken from the control sample are grey plus symbols, SF spaxels taken from AGN hosts are light blue circles. Regressions over each data set are labelled. Squares represent the mean value with standard deviations of 20 linearly spaced bins over $\Sigma\mathrm{SFR}_{\mathrm{Gas}}$ (values below 0.5 and 99.5 of the q-th percentile were removed) considering all spaxels (SF from Ctrl and SF AGNs). Density histograms of both samples are also shown. The cyan rectangle represents the high $\Sigma\mathrm{SFR}/M_{\star}$ region, namely: $\log(\Sigma\mathrm{SFR}_g/M_{\star}) > -8.2$ and $\log(\Sigma\mathrm{SFR}_{\star}/M_{\star}) > -7.8$.

extinction derived for the gas $A_{V,g}$ is consistently larger than $A_{V,\star}$ by a multiplicative factor ranging from 2.64 to 2.85, depending on the sample. The larger values obtained for the gas extinction than those of the stars are in agreement with the similar finding of Calzetti, Kinney & Storchi-Bergmann (1994), who have analysed *IUE* UV and optical spectra of 39 starburst and blue compact galaxies and studied the average properties of dust extinction. They found that the optical depth obtained via Balmer emission lines is about twice that obtained via the underlying continuum around these lines. They interpret this difference as a consequence of the fact that the hot ionizing stars are associated with dustier regions than that of older (colder) stars that contribute also to the continuum.

We thus interpret the difference we found for the extinction of the stellar population via full spectral fitting and that of the gas as being due to the fact that STARLIGHT works with a single reddening for all the population components (e.g. the final mix is reddened). Since the old component contributes significantly ($\gtrsim$60 per cent) to the integrated light in almost all spaxels (see fig. 1 of Mallmann et al. 2018), its reddening dominates the reddening of the final integrated model spectrum. The reddening of this older and cooler underlying population is therefore lower than that of the younger components, which are buried deeper in the dust (and are responsible to ionize the line-emitting gas).

5 CONCLUSIONS

We have presented a comparison between SFR surface densities obtained from spectral synthesis of the stellar population $\Sigma\mathrm{SFR}_{\star}$ and

Downloaded from https://academic.oup.com/mnras/article/501/3/4064/6043241 by Universidade Federal do Rio Grande do Sul user on 07 April 2021

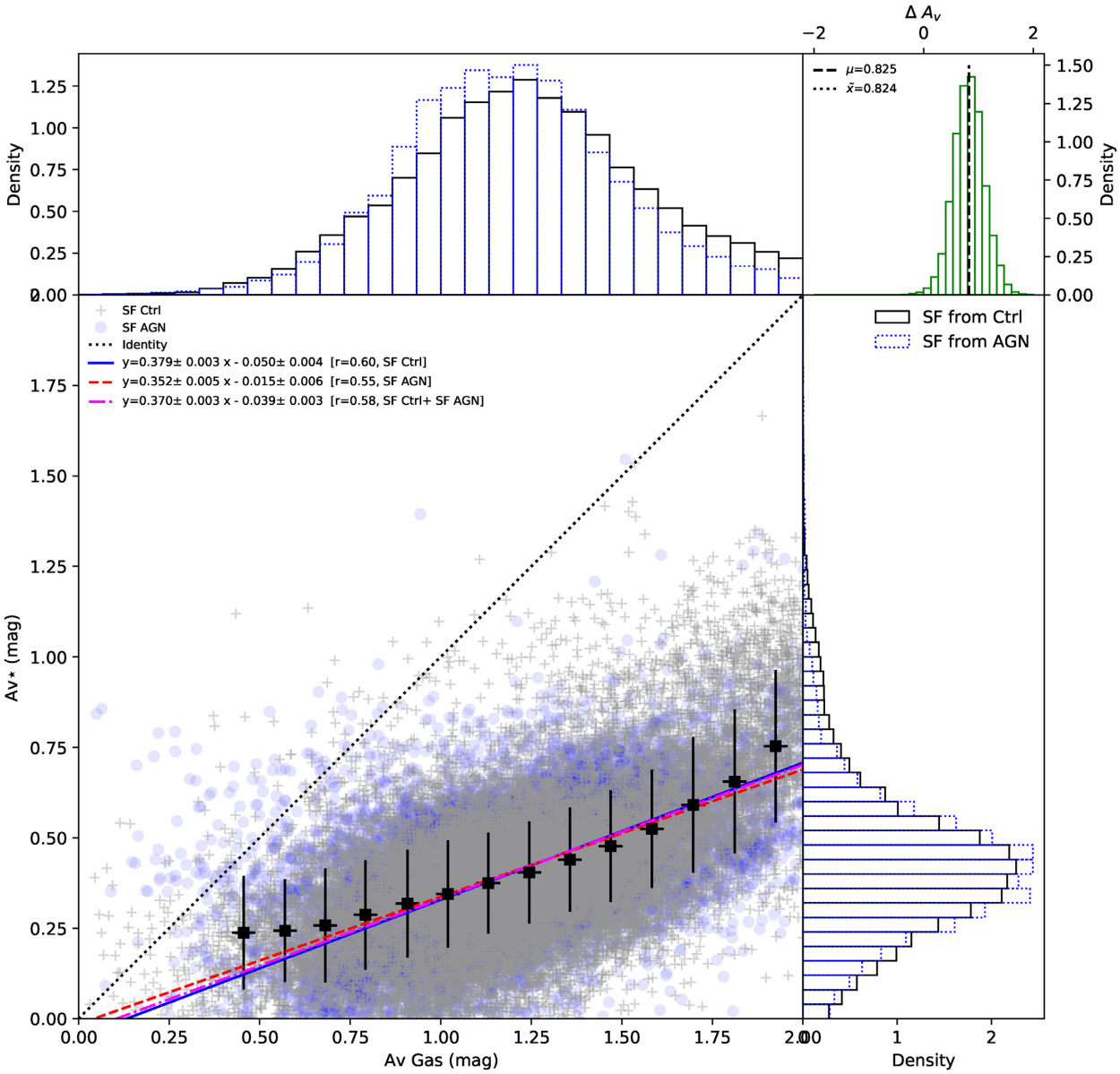

Figure 5. Gas reddening *versus* full spectral fitting reddening. Spaxels with SF line ratios taken from the control sample are grey plus symbols, SF spaxels taken from AGN hosts are light blue circles. Regressions over each data set are labelled. Squares represent the mean value with standard deviations of 20 linearly spaced bins over $\Sigma\mathrm{SFR}_{\mathrm{Gas}}$ (values below 0.5 and 99.5 of the q-th percentile were removed) considering all spaxels (SF from Ctrl and SF AGNs). Density histograms of both samples are also shown.

from the Hα gas emission $\Sigma\mathrm{SFR}_{\mathrm{Gas}}$ for an updated sample of 170 AGN and 291 control galaxies relative to our initial sample defined by Rembold et al. (2017). We have used the corresponding MaNGA datacubes selecting only spaxels high SNR continuum, with strong emission lines, and showing star-forming line ratios as obtained from diagnostic diagrams. Our main results can be summarized as follows.

(i) The $\Sigma\mathrm{SFR}_{\star}$ over the last 20 Myr and $\Sigma\mathrm{SFR}_{\mathrm{Gas}}$ show the best correlation among all tested age bins, both including in the analysis the SF spaxels from AGN hosts or only those from control galaxies. The transformation equation is $\log(\Sigma\mathrm{SFR}_{\star}) = (0.872 \pm 0.004)\log(\Sigma\mathrm{SFR}_{\mathrm{Gas}}) - (0.075 \pm 0.006)$ or $\log(\Sigma\mathrm{SFR}_{\mathrm{Gas}}) = (1.147 \pm 0.005)\log(\Sigma\mathrm{SFR}_{\star}) + (0.086 \pm 0.080)$. This result opens a new way to obtain the SFRs in AGN hosts, even in the NLR and ENLR, were the AGN dominates the excitation of the emission lines and the SFR cannot be obtained directly from the H I line fluxes.

(ii) A few AGN hosts show an excess of ΣSFR relative to the rest of the sample that we tentatively attribute to a larger gas reservoir and SF efficiency. Coincidentally, these AGNs seem to have close neighbours, thus the interaction could have boosted the SF (to be further investigated due to the small size of the sample).

(iii) We found that the visual extinction $A_{V,g}$ derived from the Balmer decrement is 2.63 to 2.86 times larger than the extinction derived from the stellar population synthesis, $A_{V,\mathrm{star}}$. This result is in agreement with previous literature results based on much smaller samples. We interpret the difference as being due to the fact that

Downloaded from https://academic.oup.com/mnras/article/501/3/4064/6043241 by Universidade Federal do Rio Grande do Sul user on 07 April 2021

STARLIGHT works with a single reddening for all populations, and the reddening of the stellar content is dominated by the older population that is less extinct than the young stellar population that would be similarly extinct as the star-forming gas.

The transformation equation presented here (equation 10) can be used to obtain the gas ΣSFR in AGN hosts via stellar population synthesis using the full spectral fitting. Since the synthesis allows disentangling the contributions of the stellar populations from that of the AGN featureless continuum, it is possible to obtain the ΣSFRs that one would derive for the gas emission, even in regions dominated by AGN excitation. The obtained SFRs in AGN hosts can then be compared with those obtained for control galaxies to investigate the effect of AGN on the surrounding stellar population as well as be compared (and incorporated) with the SFR values predicted as due to AGN feedback effects on the host galaxies in cosmological simulations.

ACKNOWLEDGEMENTS

We thank an anonymous referee for comments and suggestions that have helped improving the text. RR thanks CNPq, CAPES, and FAPERGS for financial support, as well as to Marina Trevisan for useful discussions of the present results. RAR thanks partial financial support from Conselho Nacional de Desenvolvimento Científico e Tecnológico (202582/2018-3 and 302280/2019-7) and Fundação de Amparo à pesquisa do Estado do Rio Grande do Sul (17/2551-0001144-9 and 16/2551-0000251-7). MB acknowledges support from FONDECYT regular grant 1170618. GSC acknowledges the support from CONICYT FONDECYT project no. 3190561.

SDSS is managed by the Astrophysical Research Consortium for the Participating Institutions of the SDSS Collaboration including the Brazilian Participation Group, the Carnegie Institution for Science, Carnegie Mellon University, the Chilean Participation Group, the French Participation Group, Harvard-Smithsonian Center for Astrophysics, Instituto de Astrofisica de Canarias, The Johns Hopkins University, Kavli Institute for the Physics and Mathematics of the Universe (IPMU) / University of Tokyo, the Korean Participation Group, Lawrence Berkeley National Laboratory, Leibniz Institut für Astrophysik Potsdam (AIP), Max-Planck-Institut für Astronomie (MPIA Heidelberg), Max-Planck-Institut für Astrophysik (MPA Garching), Max-Planck-Institut für Extraterrestrische Physik (MPE), National Astronomical Observatories of China, New Mexico State University, New York University, University of Notre Dame, Observatório Nacional / MCTI, The Ohio State University, Pennsylvania State University, Shanghai Astronomical Observatory, United Kingdom Participation Group, Universidad Nacional Autónoma de México, University of Arizona, University of Colorado Boulder, University of Oxford, University of Portsmouth, University of Utah, University of Virginia, University of Washington, University of Wisconsin, Vanderbilt University, and Yale University.

This research made use of ASTROPY,[4] a community-developed core Python package for Astronomy (Astropy Collaboration 2013, 2018).

DATA AVAILABILITY

The data underlying this article are available under SDSS collaboration rules, and the by products will be shared on reasonable request to the corresponding author.

[4]http://www.astropy.org

REFERENCES

Cherinka B. et al., 2019, AJ, 158, 74
Cid Fernandes R., 2018, MNRAS, 480, 4480
Cid Fernandes R., Gu Q., Melnick J., Terlevich E., Terlevich R., Kunth D., Rodrigues Lacerda R., Joguet B., 2004, MNRAS, 355, 273
Cid Fernandes R., Mateus A., Sodré L., Stasińska G., Gomes J. M., 2005, MNRAS, 358, 363
Cid Fernandes R. et al., 2013, A&A, 557, A86
Cid Fernandes R. et al., 2014, A&A, 561, A130
Crain R. A. et al., 2015, MNRAS, 450, 1937
Croton D. J. et al., 2006, MNRAS, 365, 11
Daddi E. et al., 2007, ApJ, 670, 156
Davison A. C., Hinkley D. V., 1997, Bootstrap Methods and Their Application, Cambridge Univ. Press, Cambridge
Domínguez A. et al., 2013, ApJ, 763, 145
Drory N. et al., 2015, AJ, 149, 77
El-Badry K., Wetzel A., Geha M., Hopkins P. F., Kereš D., Chan T. K., Faucher-Giguère C.-A., 2016, ApJ, 820, 131
Fabian A. C., 2012, ARA&A, 50, 455
Fouque P., Gourgoulhon E., Chamaraux P., Paturel G., 1992, A&AS, 93, 211
Gallagher R., Maiolino R., Belfiore F., Drory N., Riffel R., Riffel R. A., 2019, MNRAS, 485, 3409
González Delgado R. M., Cerviño M., Martins L. P., Leitherer C., Hauschildt P. H., 2005, MNRAS, 357, 945
González Delgado R. M. et al., 2016, A&A, 590, A44
Granato G. L., De Zotti G., Silva L., Bressan A., Danese L., 2004, ApJ, 600, 580
Gunn J. E. et al., 2006, AJ, 131, 2332
Hao C.-N., Kennicutt R. C., Johnson B. D., Calzetti D., Dale D. A., Moustakas J., 2011, ApJ, 741, 124
Hopkins P. F., 2012, MNRAS, 420, L8
Ishibashi W., Fabian A. C., 2012, MNRAS, 427, 2998
Kauffmann G. et al., 2003a, MNRAS, 341, 54
Kauffmann G. et al., 2003b, MNRAS, 346, 1055
Kennicutt R. C., Jr, 1998, ARA&A, 36, 189
Kennicutt R. C., Evans N. J., 2012, ARA&A, 50, 531
Kennicutt R. C., Jr et al., 2009, ApJ, 703, 1672
King A., Pounds K., 2015, ARA&A, 53, 115
Law D. R. et al., 2015, AJ, 150, 19
Law D. R. et al., 2016, AJ, 152, 83
Lin L. et al., 2019, ApJ, 884, L33
Lintott C. J. et al., 2008, MNRAS, 389, 1179
Lintott C. et al., 2011, MNRAS, 410, 166
McAlpine S. et al., 2016, Astron. Comput., 15, 72
Mallmann N. D. et al., 2018, MNRAS, 478, 5491
Muzzin A. et al., 2013, ApJ, 777, 18
Nayakshin S., Zubovas K., 2012, MNRAS, 427, 372
Nelson D. et al., 2015, Astron. Comput., 13, 12
Nelson D. et al., 2019, MNRAS, 490, 3234
Noeske K. G. et al., 2007, ApJ, 660, L47
Osterbrock D. E., Ferland G. J., 2006, Astrophysics of Gaseous Nebulae and Active Galactic Nuclei, 2nd edn. University Science Books, Mill Valley, CA
Owen A., 2007, Contemp. Math., 443
Peterken T., Merrifield M., Aragón-Salamanca A., Fraser-McKelvie A., Avila-Reese V., Riffel R., Knapen J., Drory N., 2020, MNRAS, 495, 3387
Rees M. J., 1989, MNRAS, 239, 1P
Rembold S. B. et al., 2017, MNRAS, 472, 4382
Riffel R., Pastoriza M. G., Rodríguez-Ardila A., Maraston C., 2008, MNRAS, 388, 803
Riffel R., Pastoriza M. G., Rodríguez-Ardila A., Bonatto C., 2009, MNRAS, 400, 273
Riffel R. A., Zakamska N. L., Riffel R., 2020, MNRAS, 491, 1518
Rosario D. J., Burtscher L., Davies R., Genzel R., Lutz D., Tacconi L. J., 2013, ApJ, 778, 94

Downloaded from https://academic.oup.com/mnras/article/501/3/4064/6043241 by Universidade Federal do Rio Grande do Sul user on 07 April 2021

Rosario D. J., Mendel J. T., Ellison S. L., Lutz D., Trump J. R., 2016, MNRAS, 457, 2703
Rosario D. J. et al., 2018, MNRAS, 473, 5658
Ruschel-Dutra, 2020, Danielrd6/Ifscube v1.0, Zenodo
Salim S., Boquien M., Lee J. C., 2018, ApJ, 859, 11
Schaye J. et al., 2015, MNRAS, 446, 521
Smee S. A. et al., 2013, AJ, 146, 32
Speagle J. S., Steinhardt C. L., Capak P. L., Silverman J. D., 2014, ApJS, 214, 15
Springel V. et al., 2005, Nature, 435, 629
Stasińska G., Costa-Duarte M. V., Vale Asari N., Cid Fernandes R., Sodré L., 2015, MNRAS, 449, 559
Trussler J., Maiolino R., Maraston C., Peng Y., Thomas D., Goddard D., Lian J., 2020, MNRAS, 491, 5406
van der Wel A. et al., 2014, ApJ, 788, 28
Vazdekis A., Sánchez-Blázquez P., Falcón-Barroso J., Cenarro A. J., Beasley M. A., Cardiel N., Gorgas J., Peletier R. F., 2010, MNRAS, 404, 1639
Vazdekis A., Koleva M., Ricciardelli E., Röck B., Falcón-Barroso J., 2016, MNRAS, 463, 3409
Vogelsberger M. et al., 2014, Nature, 509, 177
Von Der Linden A., Best P. N., Kauffmann G., White S. D. M., 2007, MNRAS, 379, 867
Wake D. A. et al., 2017, AJ, 154, 86
Walcher J., Groves B., Budavári T., Dale D., 2011, Astrophys. Space Sci., 331, 1
Wang X., Loeb A., 2018, New Astron., 61, 95
Weinberger R. et al., 2017, MNRAS, 465, 3291
Westfall K. B. et al., 2019, AJ, 158, 231
Wetzel A. R., Tinker J. L., Conroy C., 2012, MNRAS, 424, 232
White R. A., Bliton M., Bhavsar S. P., Bornmann P., Burns J. O., Ledlow M. J., Loken C., 1999, AJ, 118, 2014
Yan R. et al., 2016a, AJ, 151, 8
Yan R. et al., 2016b, AJ, 152, 197
Zhuang M.-Y., Ho L. C., 2020, ApJ, 896, 108
Zhuang M.-Y., Ho L. C., Shangguan J., 2019, ApJ, 873, 103
Zhuang M.-Y., Ho L. C., Shangguan J., 2021, ApJ, 906, 38
Zubovas K., Bourne M. A., 2017, MNRAS, 468, 4956
Zubovas K., Nayakshin S., King A., Wilkinson M., 2013, MNRAS, 433, 3079

APPENDIX: INDIVIDUAL MAPS

Here, we present individual maps for the four high ΣSFR/M$_\star$ ratio, in left from top to bottom Av$_{gas}$, Av$_\star$, Av$_{gas}$/ Av$_\star$ and in right side from top to bottom SFR$_{\rm gas}$, SFR$_\star$, SFR$_{\rm gas}$/ SFR$_\star$ note that a direct comparison of both quantities in individual galaxies is possible because the spaxels have the same area and that the ratio is showing how both quantities compare.

Downloaded from https://academic.oup.com/mnras/article/501/3/4064/6043241 by Universidade Federal do Rio Grande do Sul user on 07 April 2021

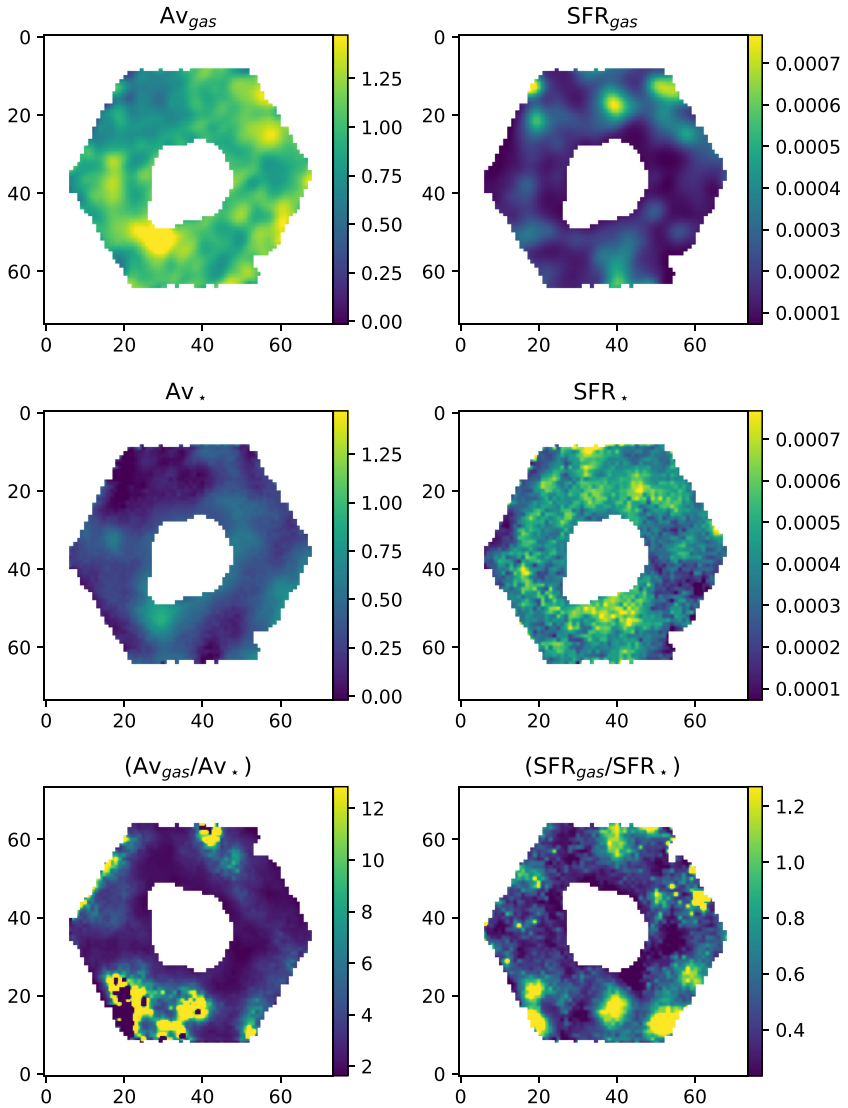

Figure A1. Individual maps for the four high ΣSFR/M$_\star$ for MANGAID 1-189584. Left side: from top to bottom A$_{Vg}$, A$_{V\star}$, Av$_{gas}$/ Av$_\star$. Right side: from top to bottom SFR$_g$, SFR$_\star$, SFR$_g$/ SFR$_\star$. SFR are givens in M$_\odot$ yr^{-1} and A$_V$ in mag.

Downloaded from https://academic.oup.com/mnras/article/501/3/4064/6043241 by Universidade Federal do Rio Grande do Sul user on 07 April 2021

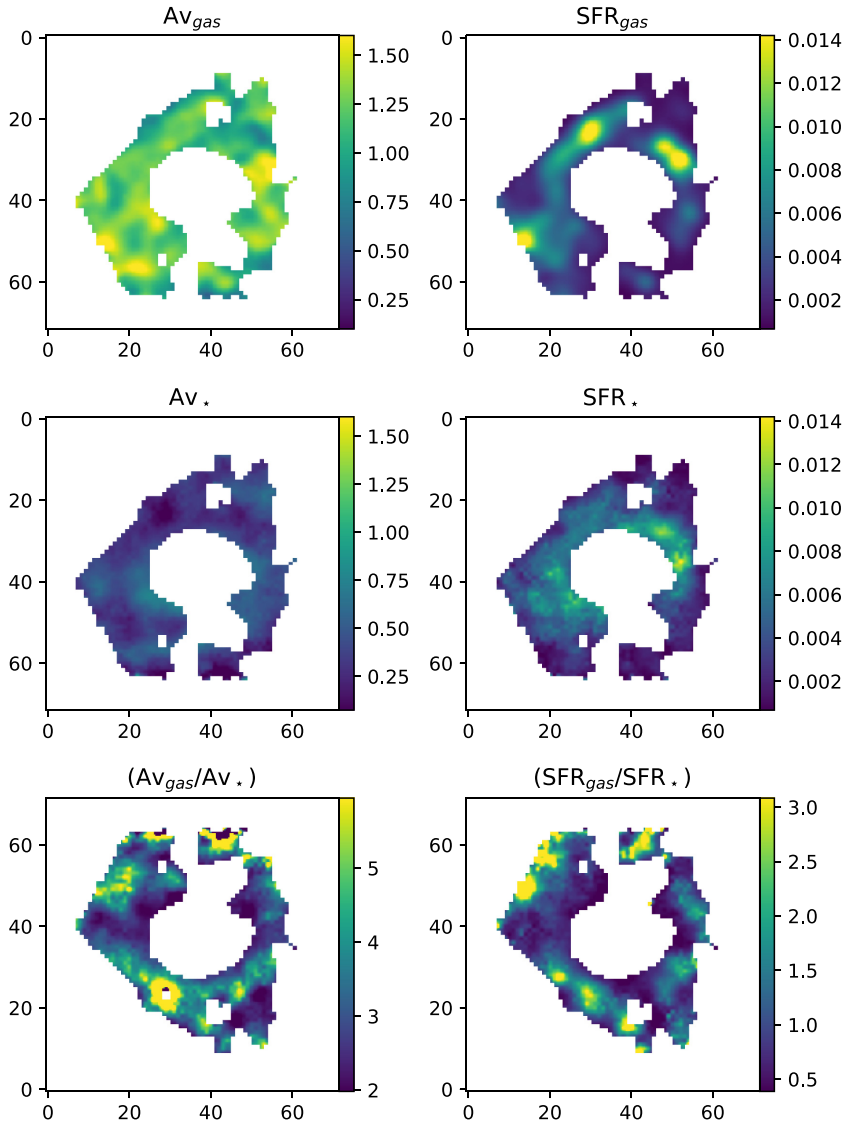

Figure A2. Same as Fig. A1 but for 1-604022.

Downloaded from https://academic.oup.com/mnras/article/501/3/4064/6043241 by Universidade Federal do Rio Grande do Sul user on 07 April 2021

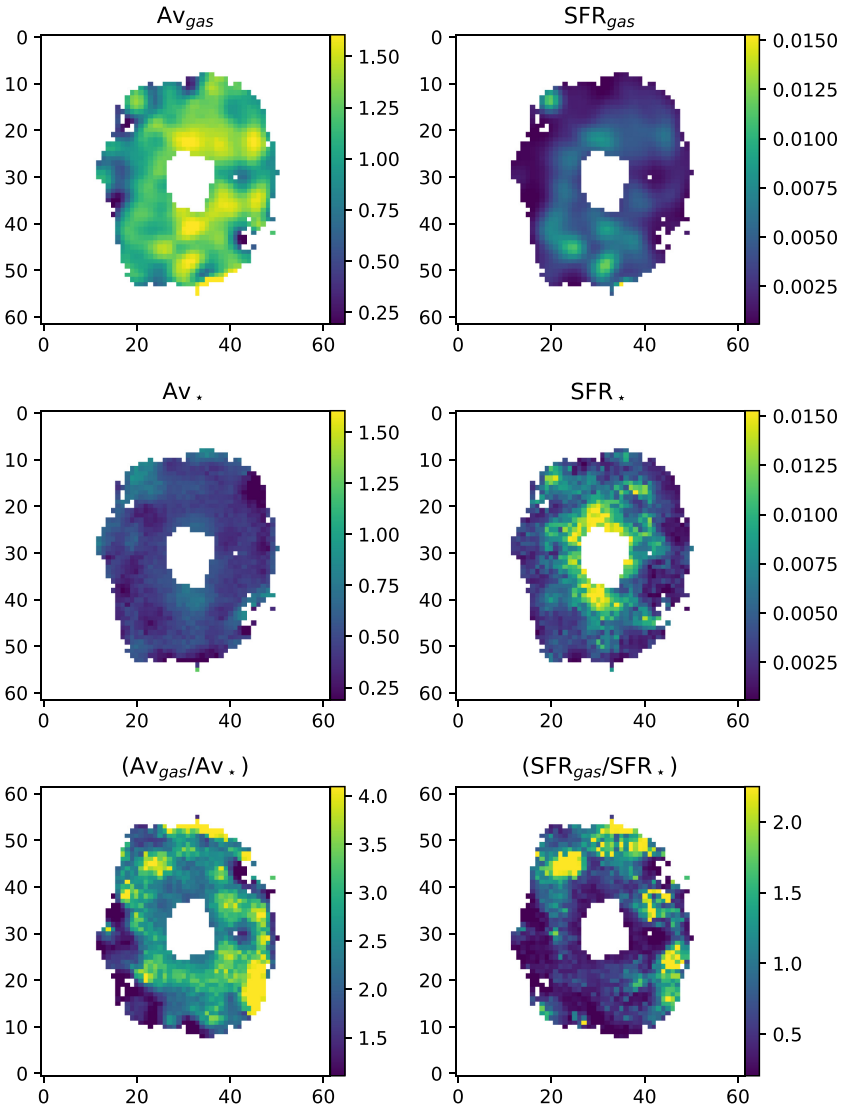

Figure A3. Same as Fig. A1 but for 1-603941.

Downloaded from https://academic.oup.com/mnras/article/501/3/4064/6043241 by Universidade Federal do Rio Grande do Sul user on 07 April 2021

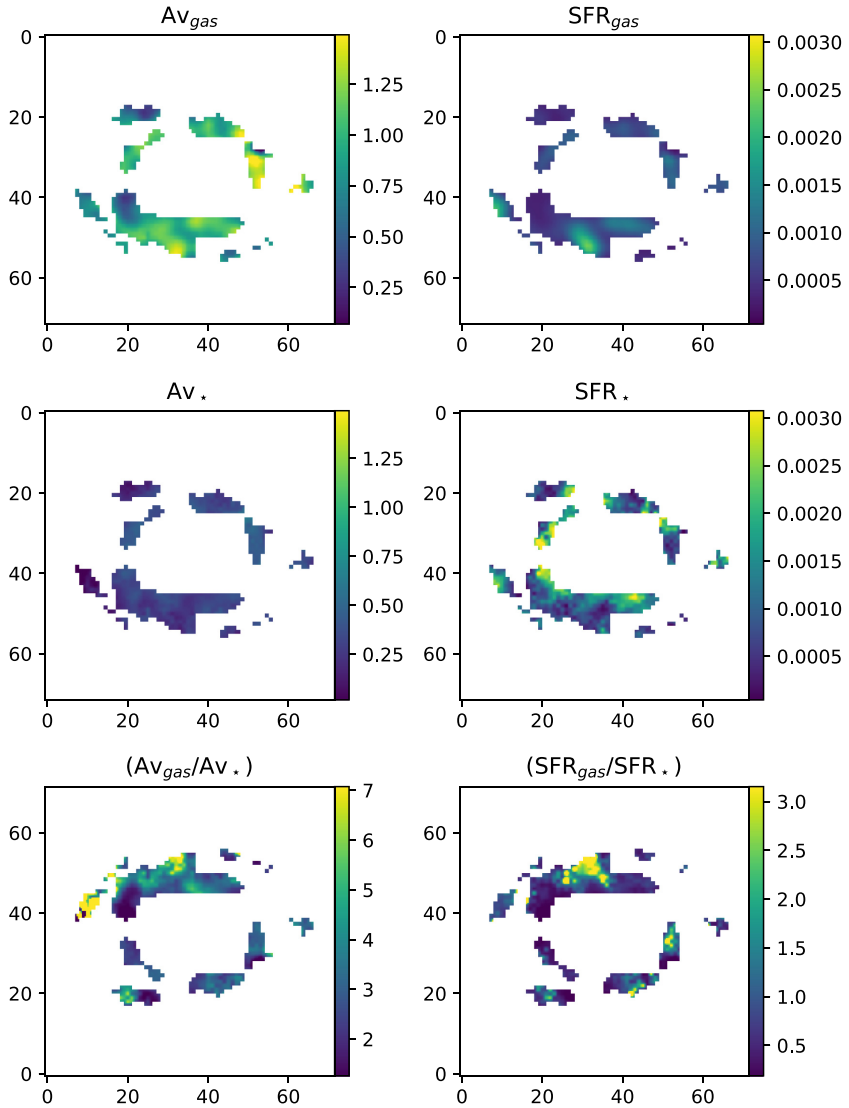

Figure A4. Same as Fig. A1 but for 1-420924.

This paper has been typeset from a TEX/LATEX file prepared by the author.

Downloaded from https://academic.oup.com/mnras/article/501/3/4064/6043241 by Universidade Federal do Rio Grande do Sul user on 07 April 2021